Monthly Notices
of the
ROYAL ASTRONOMICAL SOCIETY

MNRAS **476,** 1021–1035 (2018)
Advance Access publication 2018 January 29

doi:10.1093/mnras/sty231

Ultrafast outflows disappear in high-radiation fields

C. Pinto,[1⋆] W. Alston,[1] M. L. Parker,[1] A. C. Fabian,[1] L. C. Gallo,[2] D. J. K. Buisson,[1] D. J. Walton,[1] E. Kara,[3] J. Jiang,[1] A. Lohfink[1,4] and C. S. Reynolds[3,5]

[1]*Institute of Astronomy, Madingley Road, Cambridge CB3 0HA, UK*
[2]*Department of Astronomy and Physics, Saint Mary's University, 923 Robie Street, Halifax, NS B3H 3C3, Canada*
[3]*Department of Astronomy, University of Maryland, College Park, MD 20742-2421, USA*
[4]*Department of Physics, Montana State University, PO Box 173840, Bozeman, MT 59717-3840, USA*
[5]*Joint Space Science Institute, University of Maryland, College Park, MD 20742, USA*

Accepted 2018 January 22. Received 2018 January 18; in original form 2017 August 30

ABSTRACT

Ultrafast outflows (UFOs) are the most extreme winds launched by active galactic nuclei (AGN) due to their mildly relativistic speeds (∼0.1–0.3c) and are thought to significantly contribute to galactic evolution via AGN feedback. Their nature and launching mechanism are however not well understood. Recently, we have discovered the presence of a variable UFO in the narrow-line Seyfert 1 IRAS 13224−3809. The UFO varies in response to the brightness of the source. In this work we perform flux-resolved X-ray spectroscopy to study the variability of the UFO and found that the ionization parameter is correlated with the luminosity. In the brightest states the gas is almost completely ionized by the powerful radiation field and the UFO is hardly detected. This agrees with our recent results obtained with principal component analysis. We might have found the tip of the iceberg: the high ionization of the outflowing gas may explain why it is commonly difficult to detect UFOs in AGN and possibly suggest that we may underestimate their actual feedback. We have also found a tentative correlation between the outflow velocity and the luminosity, which is expected from theoretical predictions of radiation-pressure-driven winds. This trend is rather marginal due to the Fe XXV–XXVI degeneracy. Further work is needed to break such degeneracy through time-resolved spectroscopy.

Key words: accretion, accretion discs – black hole physics – galaxies: Seyfert.

1 INTRODUCTION

Active galactic nuclei (AGN) are powered by accretion on to supermassive black holes (SMBHs) with conversion of gravitational energy into vast amounts of radiation emitted over the entire electromagnetic spectrum. The energy throughput of AGN can regulate the growth of their host galaxies through the process known as AGN feedback (e.g. Fabian 2012 and references therein). Gas outflows in the form of winds and powerful jets release a significant amount of energy and momentum into the interstellar medium (ISM) that can expel the gas otherwise used to generate new stars. Alternatively, AGN outflows may trigger star formation by compressing the gas within the process known as positive feedback (see e.g. Maiolino et al. 2017). Ultrafast outflows (UFOs; e.g. Cappi et al. 2009) are the most extreme among the AGN winds for their mildly relativistic speeds ($\gtrsim$10 000 km s^{-1} or 0.03c) and amount of energy ($\gtrsim 0.05 L_{\rm Edd}$). These extreme winds are believed to originate from the accretion disc within a hundred gravitational radii from the black hole.

UFOs are commonly detected through high-excitation Fe XXV–XXVI absorption lines in the hard X-ray band (7–10 keV; see e.g. Tombesi et al. 2010 and references therein). This energy band is very useful because of the much lower confusion with absorption from low-velocity warm absorbers commonly found in Seyfert galaxies. Warm absorbers imprint strong absorption features in the soft X-ray band due to their lower ionization parameter, but their contribution to feedback is small (see e.g. Krongold et al. 2007 and references therein). Moreover, the Fe XXV–XXVI lines are the strongest absorption lines produced at high ionization, which is expected for winds originating in the innermost hot regions of the accretion discs. However, the presence of reflection features (e.g. reprocessing of the primary emission from the accretion disc) may complicate the identification of UFO Fe K absorption lines (see e.g. Gallo and Fabian 2011).

The soft X-ray band (∼0.3–2 keV) also provides a useful tool to search for extreme winds, but care has to be taken in distinguishing UFO features from absorption lines produced by the Galactic ISM (e.g. Pinto et al. 2013) and warm absorbers present near the X-ray source (e.g. Porquet and Dubau 2000). There are recent UFO detections in ultraluminous X-ray sources in the soft band with the high-resolution Reflection Grating Spectrometers (RGSs) onboard

⋆ E-mail: cpinto@ast.cam.ac.uk

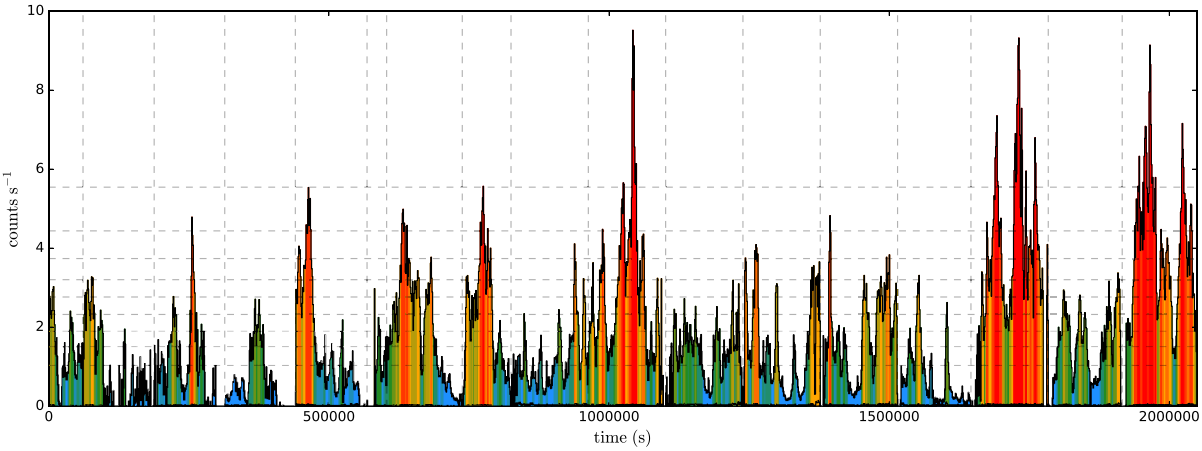

Figure 1. EPIC-pn light curve of all the observations in the 0.3–10.0 keV energy range. The vertical lines indicate the start and the end of each observation. The horizontal lines and the colours show the thresholds of the flux intervals. Flux thresholds for 10 flux regimes were chosen in order have comparable statistics. Time gaps between the observations are not shown. For more detail see text and Table 1.

XMM–Newton (Pinto, Middleton & Fabian 2016; Kosec et al. 2018) and several claims in AGN high-resolution spectra (e.g. Gupta et al. 2013; Pounds 2014; Gupta, Mathur & Krongold 2015; Longinotti et al. 2015; Reeves et al. 2016). These detectors and the gratings onboard *Chandra* provide the highest spectral resolution and resolving power in the X-ray band, which is very useful to detect and study UFOs.

UFOs show clear signatures of variability in multi-epoch deep observations with a possible transient nature (e.g. Dadina et al. 2005; Dauser et al. 2012; Zoghbi et al. 2015). The exact nature of their variability and their launching mechanism are not well understood. Variations in the column density of the absorber have been invoked to describe the variability of the wind features in PDS 456 and 1H 0707−495 (see e.g. Reeves et al. 2014; Hagino et al. 2016). In a recent very deep campaign (PI: Fabian) on the narrow-line Seyfert 1 (NLS1) IRAS 13224−3809, hereafter IRAS 13224, we have discovered a variable UFO with a clear anticorrelation between the strength of the absorption features (both in the soft and the hard X-ray bands) and the luminosity (Parker et al. 2017a, hereafter P17a). This was also confirmed by follow-up work using principal component analysis (PCA; Parker et al. 2017b, hereafter P17b). Our results argued in favour of a change in the ionization state of the outflowing gas with values sufficiently high in the brightest states that the gas is almost completely ionized and any absorption features are significantly weakened.

In this work we have performed flux-resolved X-ray spectroscopy to study the variability of the UFO and confirmed that its variability can be explained in terms of increase in the ionization parameter with the luminosity. This was possible through the combination of the high effective area of the CCD detectors and the high spectral resolution of the gratings onboard *XMM–Newton*.

This paper is structured as follows. In Section 2 we report some well-known characteristics of IRAS 13224 that motivate us to search for evidence of winds. We present the data in Section 3 and a detailed spectral modelling in Section 4. We discuss the results and provide some insights on future missions in Section 5 and give our conclusions in Section 6.

2 IRAS 13224−3809

IRAS 13224 is a low-redshift ($z = 0.0658$) NLS1 galaxy. Such objects typically exhibit high mass accretion rates on to black holes with masses smaller than quasars (10^{6-7} M$_\odot$; see e.g. Jin et al. 2012 ; Chiang et al. 2015). The smaller masses significantly shorten the time-scales of the variability processes and facilitate detailed study with the use of a few nearby exposures. The same analysis for quasars would require several years of observations. Among the brightest nearby NLS1, IRAS 13224 has the highest X-ray variability (see e.g. Ponti et al. 2012), with luminosity jumps of two orders magnitude in the X-ray band occurring on very short time frames of just a few hours (see Fig. 1). We observed this source with a deep, 1.5 Ms, *XMM–Newton* campaign (PI: Fabian) to study its variability in great detail, particularly for its strong relativistic reflection (high-energy photons reprocessed by the inner accretion disc) and time lags between the power-law continuum and the reflection features. Additional observations totalling 500 ks are available in the *XMM–Newton* archive.[1]

The large amount of data allowed us to detect multiple absorption features produced by a $\sim$0.2c UFO totalling a significance above 7σ (P17a, P17b). We also found that the strength of the absorption features decreased with increasing luminosity. Owing to the extreme flux and absorption variability present in IRAS 13224, this data set provides us with the best framework to study the link between the source luminosity and the UFO (and its detection).

3 THE DATA

In this paper we use all *XMM–Newton* observations of IRAS 13224 including the $\sim$500 ks archival and $\sim$1.5 Ms new data. We utilize data from the broad-band (0.3–10 keV) European Photon Imaging Camera (EPIC)-pn CCD spectrometer (Turner et al. 2001) and the high-resolution RGS (0.35–1.77 keV; den Herder et al. 2001) in order to constrain the spectral shape of the source and the main characteristics of the wind with a focus on their variability.

The data reduction follows the same steps used in P17a. Briefly, we reduced the data with the latest *XMM–Newton* Science Analysis System (SAS) v15.0.0 (CALDB available on 2017 April) and the standard SAS threads. EPIC-pn data were reduced with the EPPROC task and corrected for contamination from soft-proton flares.

In order to study the variability of the UFO with the source luminosity, we split the entire data set into 10 different flux levels,

[1] https://www.cosmos.esa.int/web/xmm-newton/xsa

Table 1. EPIC-pn flux levels selection and exposure times.

Level	Minimum (counts s^{-1})	Maximum (counts s^{-1})	Frame (ks)	pn (ks)	RGS (ks)
1	–	1.135	5.04	443	572
2	1.135	1.613	1.770	197	232
3	1.613	2.023	1.543	148	196
4	2.023	2.484	1.478	120	157
5	2.484	2.895	1.386	97	118
6	2.895	3.337	1.421	93	118
7	3.337	3.884	1.375	69	101
8	3.884	4.605	1.470	67	81
9	4.605	5.761	1.933	53	75
10	5.761	–	3.0	37	42

Note. The frame duration refers to the average length of each section in the EPIC-pn light curve for a given flux interval; the total exposure is the time integration for each flux interval along all archival and new pn/RGS observations.

such that the total number of counts in each of the 10 spectra is comparable. We pursued this by extracting a light curve for each observation and merging them into an overall light curve that is then divided into 10 flux intervals (see Fig. 1 and Table 1). We used the standard threads of the *XMM–Newton*/SAS[2] software.

For each flux interval, we extracted EPIC-pn spectra from within a circular region of 1 arcmin diameter centred on the emission peak. The background spectra were extracted from within a larger circle in a nearby region on the same chip, but away from the readout direction and the high copper background (Lumb et al. 2002). We also tested three other background regions on different chips to confirm that the background does not produce instrumental features.

The RGS data reduction was performed with RGSPROC. We extracted the first-order RGS spectra in a cross-dispersion region of 1 arcmin width, centred on the emission peak, and extracted the background spectra by selecting photons beyond the 98 per cent of the source point spread function. For completeness, we checked that the background spectra were consistent with blank field observations.

We stacked EPIC-pn and RGS 1–2 spectra from time intervals with same flux level and obtain 20 final spectra (one EPIC-pn and one RGS for each flux level). Each pn flux-resolved spectrum has approximately 290 000 counts, whilst its corresponding RGS spectrum has 33 000 counts. The exposure times for all spectra are shown in Table 1. We note that the RGS exposure is actually double in the wavelength ranges common to the RGS 1 and 2 detectors (5.2–10.6, 13.8–20.0, and 24.1–37.3 Å); RGS 1 misses the 10.6–13.8 Å chip, whilst RGS 2 misses the 20.0–24.1 Å chip. The RGS exposure time for each flux interval accounts for the chip losses and the stacking of RGS 1 and 2. This explains the different exposure times in Table 1.

We do not use data from the MOS 1 and 2 cameras because each has 3–4 times less effective area (and even less above 8 keV) than pn, which alone contains the vast majority of the counts. We grouped the pn spectra in bins with a signal-to-noise ratio (S/N) of at least 6 and use χ^2 statistics. Throughout the paper we adopt 1σ error bars. We perform all spectral fits with the new SPEX code[3] v3.03.

The EPIC-pn and RGS flux-resolved spectra are shown in Figs A1 and A3, respectively. The main signature of the UFO in the RGS spectrum is a broad O VIII absorption feature at around 16 Å together with some other weaker features between 10 and 13 Å, which are much more significant in deeper spectra extracted with fewer flux levels (see P17a). In the EPIC-pn spectra, the UFO can be recognized by a broad absorption feature around 8 keV plus other weaker features between 2 and 5 keV due to high-excitation states of magnesium, silicon, sulphur, argon, and calcium (P17b).

4 FLUX-RESOLVED X-RAY SPECTROSCOPY

In P17a, using the same flux levels, we found that the equivalent width (EW) of the Fe K absorption feature decreases with the source flux. It is therefore a useful exercise to apply self-consistent physical models of absorption from gas in photoionized equilibrium to understand which parameters mainly vary in the wind when the luminosity increases.

4.1 Broad-band EPIC spectral continuum

The exact knowledge of the continuum spectral components is beyond the aim of this paper and will be widely discussed in a companion paper (Jiang et al. 2017). Therefore, we adopted a phenomenological model to describe the broad-band spectral continuum, which consists of a power law (primary continuum) with slope $\Gamma \sim 2.2$–2.9, a blackbody (soft excess) with temperature $kT \sim 0.11$–0.12 keV, and two Gaussian lines relativistically broadened (i.e. multiplied by the LAOR model in SPEX with emissivity index of about 9, inclination $\sim 70^\circ$, and inner radius $1.4r_g$) to describe the main reflection features around 1 and 7 keV following the approach used by Fabian et al. (2013). The emission model is corrected for redshift and absorption due to the foreground ISM (HOT model in SPEX with column density $N_H = 6.75 \times 10^{20}$ cm^{-2} and low temperature 0.5 eV; see e.g. Pinto et al. 2013). We adopted the column density from the Willingale tool[4] to account for any contribution from both gas and molecules. The detailed spectral fits for the continuum of the 10 flux-resolved spectra are given in Appendix A and Table A1. The 10 EPIC-pn spectra are fitted simultaneously in order to better constrain the parameters of the relativistic broadening (LAOR model).

This continuum model describes the EPIC flux-resolved spectra reasonably, but strong residuals are found in terms of absorption features around 0.8 keV ($\sim$16 Å) and 8 keV (see Fig. 2), along with several weaker absorption features, which are stronger at low-flux regimes and are mainly due to absorption from the UFO as shown in P17a and P17b. The energies of the residuals agree with the blueshifted ($0.24c$) K-shell transitions of the most abundant ions in the X-ray energy band, such as O VIII, Ne X, Mg XII, and Fe XXV.

Interestingly, the O VIII absorption line is still present, though fainter, at high fluxes, whilst the iron line seems to vanish (see also Fig. A1).

Once we have obtained a reasonable description of the source continuum for each of the 10 flux regimes, we search for variability in the absorption lines produced by the UFO in the soft X-ray band with the high-resolution RGS instruments. This is particularly useful since the EPIC-pn lacks the spectral resolution necessary to resolve absorption features below 2 keV.

[2] https://www.cosmos.esa.int/web/xmm-newton/sas
[3] http://www.sron.nl/spex
[4] http://www.swift.ac.uk/analysis/nhtot/

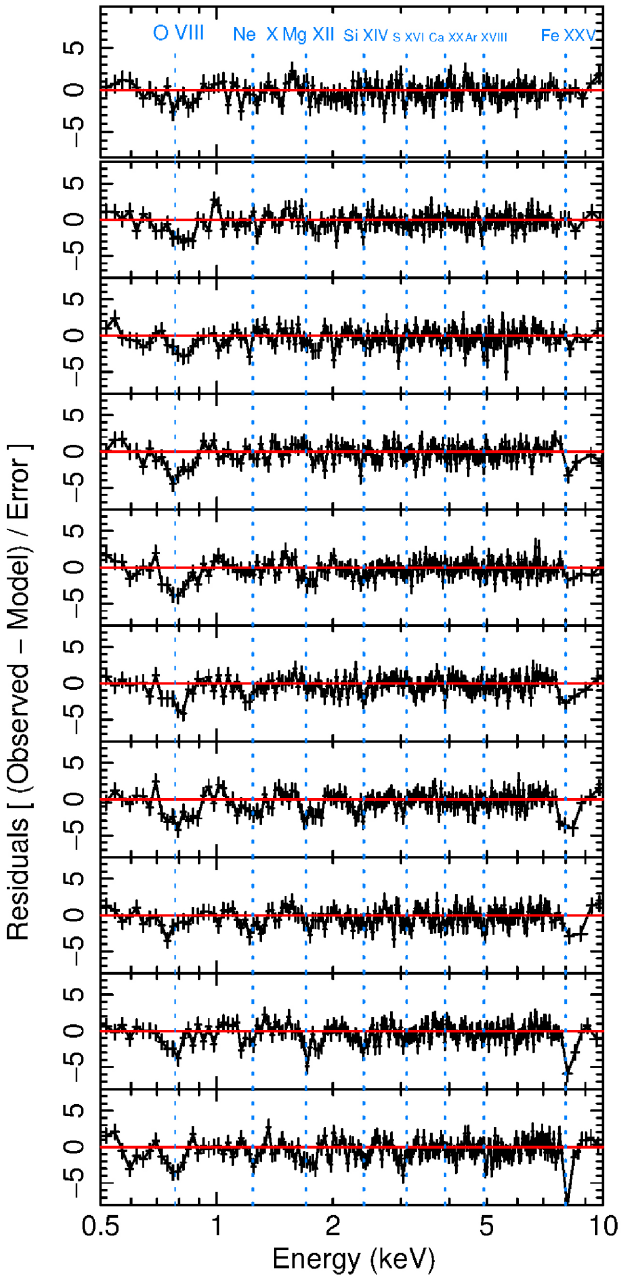

Figure 2. IRAS 13224 flux-selected EPIC-pn spectral fits (ordered according to their luminosity from bottom to top). Energy transitions of relevant ions blueshifted by 0.24c are labelled. Note the persistent O VIII absorption line compared to the strong decrease of the iron line at high fluxes.

4.2 The high-resolution RGS spectrum

At this stage we use the full resolving power of the RGS detector and therefore do not highly bin the spectra. We adopt bin size equal to 1/3 of the spectral resolution for the optimal binning (see Kaastra & Bleeker 2016) and use C-statistics. We focus on the 6–35 Å first-order RGS spectra. Below 6 Å the effective area is not well calibrated and above 35 Å the background is high.

We apply the EPIC continuum model of each flux-resolved spectrum to the corresponding RGS spectrum with the overall normalization allowed to vary to account for any uncertainty in the cross-calibration between the two instruments (in some cases up to 10 per cent). As for EPIC, the continuum spectral model describes the RGS spectrum well, although RGS does not have the same broad-band sensitivity. Therefore, the continuum model does not have a significant effect on the search for narrow lines in the RGS spectra.

Following the approach used in P17a, we search for spectral features on top of the continuum by fitting a Gaussian spanning the 6–35 Å wavelength range with increments of 0.05 Å and calculate the ΔC-statistics. We test a few different line widths obtaining consistent results: full width at half-maximum (FWHM) = 500, 1000, 5000, and 10 000 km s^{-1}. We show the results obtained with 5000 km s^{-1} in Fig. 3 because this value is similar to the velocity width measured in P17a (FWHM = $2.35\sigma_v = 2.35 \times 2000 \sim 5000$ km s^{-1}). The wavelengths are corrected for redshift ($z = 0.0658$). The source flux increases from bottom to top. The left-hand panels show the changes in the ΔC-statistics, multiplied by the sign of the normalization of the Gaussian in order to distinguish between emission and absorption lines; the right-hand panels show the ratio between the normalization of the Gaussian and its error. More detail on use of this line scan and the comparison between intrinsic and Galactic absorption lines can be found in Pinto et al. (2016).

As previously seen in P17a for three flux regimes, the 10 flux-resolved spectra show significant residuals that weaken at high fluxes. There is weak evidence of emission-like features, see Fig. 3, but they vary both in strength and position between the observations for which it is difficult to address the significance and the origin. If they are real they might be related to some reflection occurring in the disc much further away (around 1000 R_S; see e.g. Blustin & Fabian 2009), but their variability would rather suggest that they are produced by reflection of coronal photons from the inner accretion disc (García et al. 2016). We do not expect these lines to have a major effect on to the measurements of the absorption lines and their variability. The main absorption feature at 15 Å (or 16 Å, ∼0.8 keV, in the observed frame) detected in the low-flux RGS spectra resolves the residuals found in the EPIC spectra (see Fig. 2).

4.3 EPIC–RGS simultaneous fit: wind model

As noted in P17a, the absorption features detected in the RGS and EPIC spectra of IRAS 13224 are not compatible with a rest-frame absorber or a low-velocity warm absorber commonly found in Seyfert galaxies (see e.g. Krongold et al. 2007 and references therein) nor with any absorption from the foreground ISM (e.g. Pinto et al. 2013 and references therein). They are instead all consistent with an outflowing velocity of about 0.24c as shown by the blue-dotted lines in Fig. 2, which agree with an UFO nature.

An accurate modelling of a photoionized absorber requires both broad-band coverage and high spectral resolution. We therefore simultaneously fit the 10 flux-selected EPIC-pn and RGS spectra and, for consistency, we group the EPIC and RGS spectra to an S/N of at least 6 and use χ^2 statistics. We also make sure that the bin size is always of 1/3 of the spectral resolution or above. This spectral binning mainly affects the wavelength range below 10 Å and above 27 Å in the low-flux RGS spectra and does not decrease our resolving power because the UFO soft features – detectable with RGS – are between 10 and 16 Å.

As previously done in P17a, we model the absorption features with the XABS model in SPEX. This model calculates the transmission of a slab of material, where all ionic column densities are linked through a photoionization model. It is a flexible code that can reproduce photoionized plasma in different ionization fields such as in

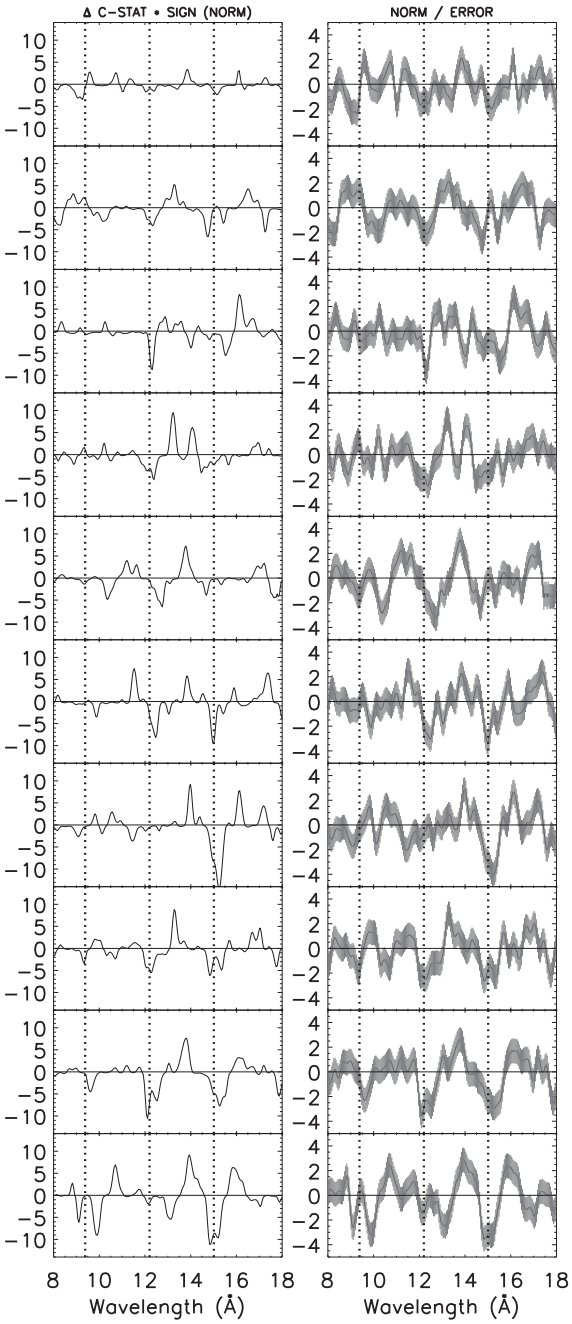

Figure 3. RGS-only line search for the 10 flux regimes from low (bottom) to high fluxes (top). The left-hand panel shows the ΔC-statistics multiplied by the sign of the line in order to distinguish both the significance and the kind (emission/absorption) of each feature. The right-hand panel shows the ratio between the normalization of the Gaussian and its error zoomed on the region with high effective area. The bands coloured in grey are the 1σ error bars. Here the wavelengths are corrected for the redshift (0.0658). The vertical dotted lines indicate the rest-frame transitions of the strongest features detected in the 2 Ms stacked spectrum (P17a).

the ISM and X-ray binaries (e.g. Pinto et al. 2012a,b). The relevant parameter is the ionization parameter

$$\xi = \frac{L_{\rm ion}}{n_{\rm H} R^2}, \quad (1)$$

with $L_{\rm ion}$ the ionizing luminosity, $n_{\rm H}$ the hydrogen number density, and R the distance from the ionizing source (see e.g. Steenbrugge et al. 2003). We apply the XABS as a multiplicative component on to all emission components:

HOT * RED * XABS * (BB + POW + LAOR * (GAUSS + GAUSS)),

which physically can be described as

ISM * REDSHIFT * WIND * (CONTINUUM + REL-BROAD * (FE L + FE K)),

where the relativistically broadened Fe L (1 keV)/Fe K (7 keV) lines and the blackbody+power-law continuum are at first absorbed by the photoionized wind, then corrected for redshift, and finally absorbed by the mainly neutral ISM in the Galaxy.

The free parameters in the XABS model are the column density, $N_{\rm H}$, and the ionization parameter, ξ. The line width, σ_v, and the line-of-sight velocity, $v_{\rm LOS}$, are tied to the values measured in P17a (2000 km s^{-1}, 0.236c, or 0.21c), with the more sensitive 2 Ms archival+new data stacked RGS–EPIC spectra. The faster (0.236c) lower ionization solution – where the Fe XXV significantly contributes to the absorption at 8 keV – is slightly preferred by the 2 Ms stacked spectrum (see P17a) and by the PCA analysis (P17b), but the alternative slower (0.21c) higher ionization model also provides reasonable fits. We therefore perform the following analysis for both solutions for completeness. At a first stage, we fixed the LOS velocities to the values measured in P17a with the time-averaged spectrum that has much higher S/N than each flux-resolved spectrum. In Table 2 we report the χ^2 values for each EPIC and RGS flux-resolved spectrum from the simultaneous fits (fast model) compared to the results obtained with the continuum model. The statistical improvements by the photoionized absorption models are plotted in Fig. 4 individually for EPIC and RGS (both fast and slow models). Spectra with best-fitting models and residuals are shown in Figs A5 and A6. The fits of the 0.236c and 0.21c solutions are remarkably similar. The parameters of the absorbers are reported in Table A2. We have confirmed the variability of the absorber with additional fits where the absorption model was fixed to that of the lowest flux spectrum and the continuum was free (see Figs A7 and A8). Deviations are found corresponding to the main transitions (blue dotted lines). We report the detail of the adopted spectral energy distribution (SED) and the ionizing flux in Appendix A and in Figs A2 and A4.

Most absorption features in each EPIC and RGS flux-resolved spectrum can be well described with one photoionized XABS absorber with a high ionization parameter ($\log \xi \sim 4$–5) and a relativistic outflow velocity of 0.236c, very similar to the results obtained in P17a and P17b. Interestingly, we do not find significant deviations

Table 2. Statistical improvements of the absorber.

	EPIC-pn			RGS		
	Continuum		Abs	Continuum		Abs
Level	χ^2	dof	$\Delta\chi^2$	χ^2	dof	$\Delta\chi^2$
1	328	177	64	377	335	28
2	254	171	64	361	322	29
3	212	166	36	448	357	15
4	258	167	54	417	364	41
5	193	163	38	418	348	27
6	203	167	44	433	371	7
7	210	158	29	468	379	12
8	229	162	16	460	353	33
9	185	164	18	473	386	25
10	174	162	5	451	392	13

Note. Each photoionized absorber has free parameters the column density and the ionization parameter (Fe XXV solution). The velocity broadening and the $v_{\rm LOS}$ are fixed to Parker et al. 2017a value. We show the $\Delta\chi^2$ trends for the Fe XXV–XXVI solutions in Fig. 4.

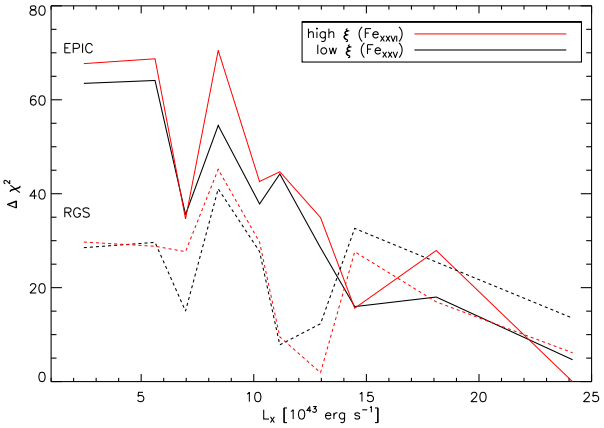

Figure 4. Statistical improvements of the absorber obtained on the flux-resolved EPIC and RGS spectra. Both the low ξ and high ξ solutions are shown, where the former one is detailed in Table 2.

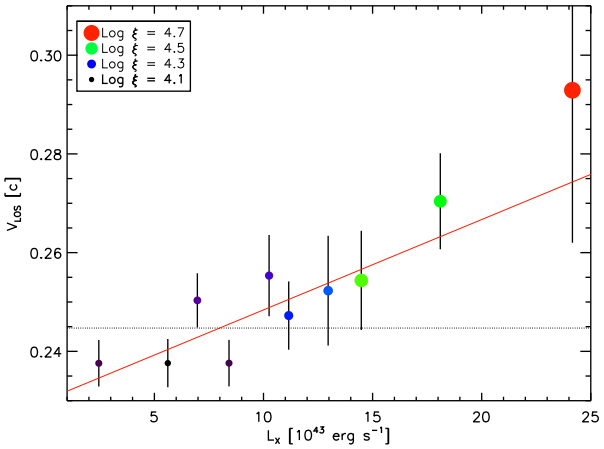

Figure 5. Line-of-sight velocity of the wind versus X-ray luminosity. The point colour and size are coded according to the value of the ionization parameter. The red solid line shows a linear fit. The horizontal line is the fit with a constant function.

in the column density of the absorber between the 10 different flux-resolved spectral fits. The values measured with the Fe XXV and Fe XXVI solutions are consistent with those reported in P17a, albeit with larger uncertainties due to the fact that we split the entire observation in 10 flux intervals.

In Jiang et al. (2017) we also use deeper spectra splitting the data in just three flux intervals and found tentative evidence of a second photoionized absorber, which marginally improves the fit of the Fe K blue wing. This absorber is not detected in our spectra due to their much shorter exposure and is not expected to affect our results.

For completeness, we have tested the effect of any warm absorber through the time-integrated stacked RGS spectrum (see P17a) and fitted it with the same continuum and UFO model used in this paper and have then added a low-velocity (0–5000 km s^{-1}) photoionized absorber with log $\xi \sim$ 1–4 (an additional XABS component). The addition of the warm absorber does not significantly improve the fit. We have also tried to remove the UFO model and fit the absorption features just with the warm absorber, but that is unsatisfactory due to the fact that no additional O VII–VIII absorption features are detected as required from a standard warm absorber model. The overall improvement of the warm absorber model (for fits without the UFO model) is ΔC/degreesoffreedom(dof) = 20/3, compared to the >150/3 for the UFO, and $\Delta C \sim$ few for each flux resolved spectrum. We obtain a 90 per cent upper limit on the column density $N_{\rm H}^{\rm WA} \lesssim 2 \times 10^{20}$ cm^{-2} for log $\xi \sim 2$. Similar results are given by a low-velocity emission component.

4.3.1 *Wind velocity versus X-ray luminosity*

Radiation-driven winds are expected to show correlation between the outflow speed and the X-ray luminosity (see e.g. Matzeu et al. 2017 and references therein). We have therefore performed a fit with free velocity among the 10 spectra, which shows velocities broadly consistent within the error bars (see Fig. 5, for the faster solution). A constant function yields $\chi^2_\nu = 2.26$ for 9 dof (p-value = 0.016), slightly improved by a velocity–luminosity linear fit ($\chi^2_\nu = 0.90$ for 8 dof, p-value = 0.52, and a slope 0.0019 ± 0.0005).

The Pearson and Spearman correlation coefficients of the (v, $L_{\rm X}$) points are 0.93 and 0.86, respectively, implying a strong correlation. We establish the significance of this correlation using a Monte Carlo approach. We simulate 10^6 equivalent sets of points, assuming that the velocity of the outflow is constant, and that the errors are Gaussian. Of these, 483 have a higher Pearson coefficient, 3595 have a higher Spearman coefficient, and 418 have both higher. These give significances of 99.95, 99.64, and 99.96 per cent, respectively. Our results agree with the trend observed in the quasar PDS 456 and a scenario of radiation-driven wind (Matzeu et al. 2017).

There is however some degeneracy between the two solutions (high Fe XXV versus high Fe XXVI) at this stage. The velocity separation between the two scenarios is within the error bars of $\sim$0.01c statistical plus the line broadening $\sim$5000 km s^{-1}. The peaks of the χ^2 distributions are separated by a few digits for some flux intervals (see e.g. Fig. 4), which weakens the trend and therefore we consider it just as tentative. It is possible that the flux selection of events at different epochs somehow smeared out the results. In a forthcoming paper we will try to obtain more information on the source variations through time-resolved spectroscopy.

4.3.2 *Wind ionization versus X-ray luminosity*

The goal of this work is to understand the behaviour of the wind across different flux states and search for any luminosity dependence. As can be seen in Table 2 and Fig. 4, the addition of a photoionized absorption model improves most of the fits whether we adopt the low or high ξ solutions. However, the largest difference in χ^2 is to be found at lower flux states, which confirms that the wind features weaken with increasing flux.

In Fig. 6, we show the ionization parameter measured for each RGS–EPIC flux-selected spectrum and the corresponding X-ray luminosity estimated between 0.3 and 10 keV totalling the contributions of the four emission components. We prefer to use the luminosities as measured with the continuum fits because they are not affected by the photoionization modelling and provide lower limits to the actual source brightness. Both the Fe XXV (filled circles) and Fe XXVI (open circles) solutions are shown. We also show the results where the line-of-sight velocity is free to vary (triangles) and where the column density is tied to the P17a value (stars).

All the spectral fits show a clear correlation between the ionization parameter and the X-ray luminosity. The origin of such trend is discussed in the following section. Here we mainly notice that a

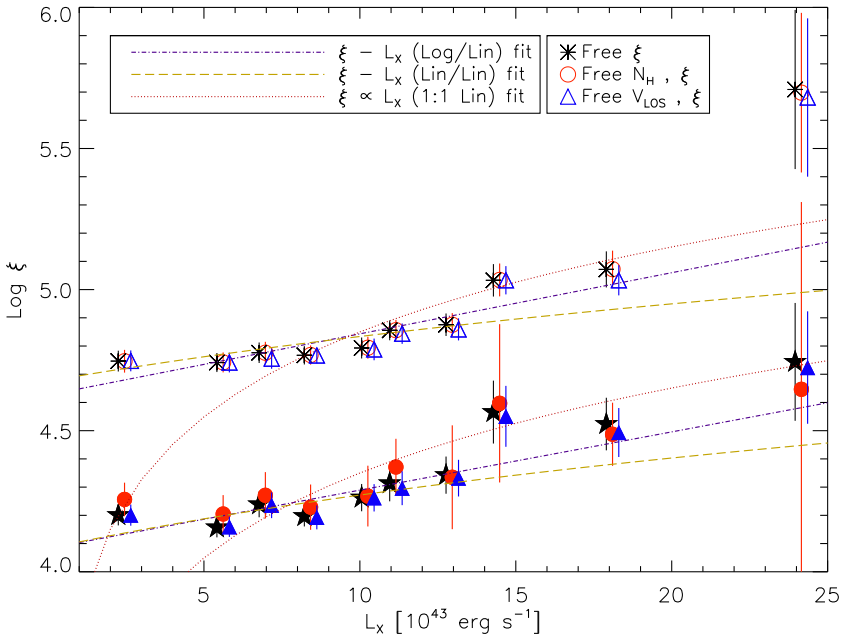

Figure 6. EPIC-pn+RGS results: ionization parameter versus X-ray luminosity. The results of both the high ξ (open points) and low ξ (filled points) models are shown along with their liner and log-linear fits (see equation 2). Stars, circles, and triangles indicate spectral fits with different free parameters. Log ξ–L_X and ξ–L_X fits are performed. The points clearly deviate from the 1:1 (dotted) line.

linear fit to the ξ–L_X points provides

$$\frac{\xi}{10^4} = (4.7 \pm 0.8) + (0.21 \pm 0.06)\frac{L_X}{10^{43}} \quad (\mathrm{Fe\,XXVI}), \tag{2}$$

$$\frac{\xi}{10^4} = (1.2 \pm 0.3) + (0.07 \pm 0.02)\frac{L_X}{10^{43}} \quad (\mathrm{Fe\,XXV}), \tag{3}$$

corresponding to $\chi^2_\nu = 2.7$ and 1.4, respectively, for 8 dof. A constant function yields significantly worse fits, $\chi^2_\nu = 5.8$ and 4.1, respectively.

The highest flux pn spectra are just above the pile-up threshold at energies below 1 keV, potentially affecting the spectrum up to 2 keV. We have repeated the simultaneous RGS and EPIC spectral fits, ignoring the EPIC data below 2 keV and covering the 0.4–2 keV band with RGS only. This test provides results on the XABS parameters consistent with those obtained using the full 0.3–10 keV EPIC spectra, which suggests that pile-up has minor effects on our analysis.

5 DISCUSSION

In P17a we have discovered mildly relativistically blueshifted absorption features in the *XMM–Newton* and *NuSTAR* spectra of IRAS 13224, which were interpreted as strong evidence for a UFO. We further found that the features weaken when the flux increases, which can be explained as a decrease of the column density or an increase of the ionization parameter. More recently, the PCA analysis of IRAS 13224 (P17b) has provided further support for the latter scenario showing, however, that the response of the absorber is not as strong as the luminosity variations.

5.1 High Eddington accretion?

Ultrafast winds are expected to be driven by radiation pressure when the compact object accretes at or above the Eddington limit (see e.g. Takeuchi, Ohsuga & Mineshige 2013). But at which Eddington rate is IRAS 13224 actually accreting?

The exact mass of the SMBH powering IRAS 13224 is not well known. For a black hole with a mass of $M_{\rm BH} = 10^7\,{\rm M}_\odot$, which is a conservative value for our source and NLS1 in general (see e.g. Chiang et al. 2015), the Eddington limit $L_{\rm Edd} = 3.2 \times 10^4 (M_{\rm BH}/{\rm M}_\odot){\rm L}_\odot$ is reached at about $1.3 \times 10^{45}\,{\rm erg\,s^{-1}}$.

We can estimate the bolometric luminosity through the hard X-ray (2–10 keV) to bolometric luminosity correction according to Vasudevan & Fabian (2007). They reported correction factors between 15 and 70 for NLS1 galaxies, which would suggest that IRAS 13224 bolometric luminosity spreads between 0.02 and $1.6 \times 10^{45}\,{\rm erg\,s^{-1}}$, with an average throughout the *XMM–Newton* observations of $\sim 3 \times 10^{44}\,{\rm erg\,s^{-1}}$. Despite systematic uncertainties this suggests that the source accretes at significant fraction of the Eddington limit and possibly surpasses it during the brightest epochs.

In a parallel paper that focuses on the continuum decomposition and variability of IRAS 13224 (Jiang et al. 2017) we use the data available on the NASA/IPAC Extragalactic Database[5] for the source from optical to hard X-rays to model the SED. The optical to hard X-ray SED is fitted with a blackbody plus power-law emission model. We estimate a range for the bolometric luminosity of $\sim$0.3–3.0 $L_{\rm Edd}$ (with the uncertainty mainly driven by the blackbody temperature adopted). This agrees with Sani et al. (2010) and the average measurements of Buisson et al. (2017) of about 70 per cent Eddington. More recently, Buisson et al. (2018) obtained tighter limits on the luminosity for the time-average SED ($\sim$0.3–1 $L_{\rm Edd} \times \frac{10^7\,{\rm M}_\odot}{M_{\rm BH}}$) using an additional blackbody for the ultraviolet (UV) emission from thin disc.

We notice that all the previous calculations make use of the observed luminosity. This will be significantly lower than the intrinsic

[5] https://ned.ipac.caltech.edu

luminosity that has to account for any X-ray absorption and scattering from the ultrafast wind. Our approach is conservative and further supports the chance that IRAS 13224 accretes beyond the Eddington limit.

We have found a correlation between the velocity of the wind and the X-ray luminosity (see Fig. 5). Our results agree with the trend observed in the quasar PDS 456 and with the scenario of a radiation-driven wind at high accretion rates (see e.g. Matzeu et al. 2017 and references therein).

5.2 Scenario 1 – wind disappearance at high flux

One of the main results from the RGS line search is that the absorption lines weaken and seem to disappear at higher luminosities (see Fig. 3). In Fig. 6 we compare the ionization parameter measured for the photoionized absorber with the corresponding luminosity of the 10 flux-resolved spectra. Whether we adopt the Fe XXV or the Fe XXVI solutions we obtain a clear correlation between the ionization parameter and the X-ray luminosity. This trend may suggest that when the source brightens, possibly due to higher accretion, the enhanced radiation field increases the ionization state of the wind, which would result in a decrease of the EWs of the X-ray lines at the same column density of the wind. It is however suspicious that the ξ–L_X relationship is not a straight line as expected from equation (1) for constant wind geometry. In particular the slope is less than unity, $\xi \propto 0.05$–$0.3\,L_X$ (see equations 2 and 3), which could suggest that the wind is either not responding on time or that something else is preventing the wind to adjust its ionization state to the luminosity variations. It is possible that only a certain fraction of the luminosity is actually 'seen' by the wind and that a significant fraction is produced in an outer, screened, region. We notice that there are some systematic uncertainties in this comparison due to the fact that we are using the observed luminosities rather than intrinsic, unabsorbed, luminosities that are not known a priori.

Naively, the Fe XXVI solution would better follow the disappearance of the lines at higher ionization states. However, the same column density for Fe XXVI would provide absorption lines weaker than for Fe XXV due to the cross-sections. The fact that the lines do not 'disappear' until the highest flux states are reached and that the O VIII is always present would suggest the opposite.

We have chosen to compare the ionization parameter, ξ, with the full-band X-ray luminosity as there are absorption features over the whole 0.3–10 keV band. However, it is interesting to compare the ξ with the luminosity of the harder band, such as 5–10 keV, which contributes most of the Fe K absorption. The variations on the luminosity are smaller, approximately twice less than the total band and, interestingly, the corresponding ξ–L_X trend can be fitted with a straight line of slope 2–4. This would suggest that some of the soft X-ray emission may not be seen from the part of the wind that affects our line of sight, particularly since the O VIII is always present.

If the wind geometry and location do not change, we can use equation (1) to place constraints on the density of the gas, which is useful to calculate the recombination time-scales of the wind. If we assume that the velocity of the wind ($\sim 0.2c$) is equal to the escape velocity, then we obtain a launching radius of about 25 Schwarzschild radii, R_S. Using equation (1) and the luminosity range of IRAS 13224 as shown in Fig. 6, we estimate a number density $n_H \gtrsim 10^{10}$ cm^{-3}. Using the ionization parameters estimated for the XABS model and the SPEX REC_TIME tool, we measure the product $n_H\, t_{rec}$ between the density and the recombination time for the most abundant ions detected in the wind such as O VIII, Mg XII, Si XIV, and Fe XXV. The ratio between the $n_H\, t_{rec}$ provided by REC_TIME and the density, n_H, yields an upper limit on the recombination time of a few seconds. This means that the wind should be able to respond almost instantaneously to the luminosity variations.

Interestingly, Gallo et al. (2004) reported doubling time-scales between 300 and 800 s during which IRAS 13224 flux change significantly (and likely even shorter in the new data; e.g. Jiang et al. 2017a). This means that at $25R_S$, which corresponds to a light travel time of 2500 s, the variations in the ionizing state might start to blur together and weaken the ξ–L_X correlation. If the absorber is closer to the ionization source the correlation should strengthen, whilst higher distances would weaken it further.

5.3 Scenario 2 – clumpy wind or variable absorption from the disc photosphere?

Alternatively, it is possible that the absorption lines weaken at high luminosities due to a smaller column density of the intervening absorber. This could happen either if the wind becomes more clumpy or if line of sight of the absorber changes with respect to that towards the X-ray source.

5.3.1 *The column density changes in a clumpy wind*

If a variation in the column density, N_H, of the wind could explain both the change in luminosity and in line strength, then we should be able to fit all the flux-resolved EPIC+RGS spectra assuming the continuum model from the brightest flux state and fit the N_H of the photoionized absorber, of course expecting to find higher N_H for fainter spectra. We have tested this scenario freezing continuum models but obtained bad fits ($\Delta\chi^2 \gtrsim 100$ each) due to the fact that the spectral shape of IRAS 13224 weakly changes from the brightest to the lowest flux (see Figs A1 and A3). We should expect spectra significantly harder at higher N_H.

If the ionization parameter of the wind does not change, then both its column density and the source luminosity have to change in order to have acceptable fits. The column density has to decrease precisely with the luminosity. We have tested this case by fitting again the 10 flux-resolved EPIC+RGS spectra by freezing the (log) ionization parameter to the average value of 4.84 obtained for the Fe XXVI solution (see e.g. Fig. 6). The continuum parameters and the column density of the absorber were free to vary. These fits are slightly worse than our standard free ξ fits with $\Delta\chi^2 \sim 10$–50 each throughout the 10 spectra. The resulting N_H–L_X trend for the 10 flux-resolved spectra is shown in Fig. 7 along with the previous results obtained with free ξ and N_H. As expected, as the source becomes brighter a decrease in the column density is required to describe the weakening of the absorption lines, providing an alternative scenario to the increase of the ionization parameter.

5.3.2 *Variable absorption from the disc photosphere*

Gallo & Fabian (2011, 2013) have shown that UFO-like absorption features can be produced if an optically thin photosphere on top of the disc absorbs the X-rays from the inner regions where most of the Fe K reprocessing (or reflection) occurs. According to this scenario the absorption applies on to the reflection (secondary) rather than the power-law (primary) component, with blueshifts caused by velocities expected in the inner accretion disc. In this case, an increase in the height of the corona would decrease light

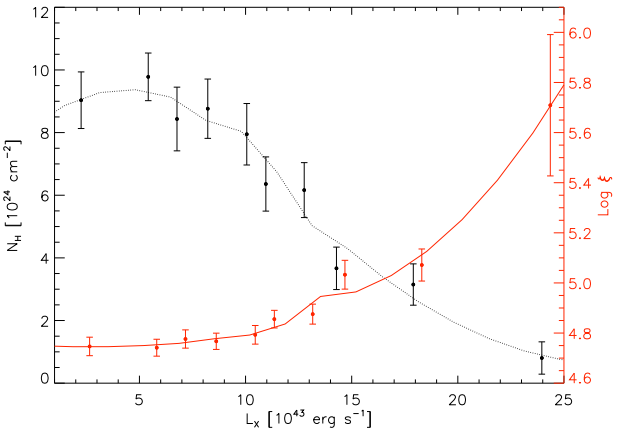

Figure 7. EPIC-pn+RGS results: column density versus luminosity (black, fixed ionization parameter) compared to ionization parameter versus luminosity (red). For high ξ, see also Section 5.3. The lines show a quadratic interpolation to both the relations. The N_H fits are slightly worse than the ξ fits by $\Delta\chi^2 \sim 10$–50.

bending, resulting in a smaller reflection fraction and therefore weaker absorption lines (see Fig. 8 and Table A1).

The actual test for this interpretation requires however an accurate calculation of the absorption through the disc atmosphere and will be done elsewhere. For the remainder of the discussion we will assume that the absorption lines are actually produced by a fast wind rather than by the disc photosphere.

5.4 Implications for AGN feedback

UFOs could provide an important contribution to AGN feedback and significantly affect the evolution of the host galaxy. Their opening angle and ejected mass are likely larger than in jets, allowing them to couple more efficiently to the ISM. According to Tombesi et al. (2010) UFOs should have a covering fraction of ∼0.4–0.6 as shown in detail for PDS 456 by Nardini et al. (2015). However, their signatures seem to vary in multi-epoch deep observations with a possible transient nature (e.g. Dadina et al. 2005; Vaughan & Uttley 2008; Dauser et al. 2012; Zoghbi et al. 2015). The exact nature of their variability is not fully understood. Some models include variable column density or covering fraction (e.g. Reeves et al. 2014; Hagino et al. 2016).

In this work we have shown that the UFO variability in IRAS 13224 – whose broad-band spectrum does not change dramatically within almost two orders of magnitude of X-ray luminosities – can be attributed to variations in the ionization parameter due to the different ionizing field. This is consistent with our recent work on PCA (P17b). The high ionization of the outflowing gas explains why it is difficult to detect the UFO in the bright states of IRAS 13224 and could potentially be one of the main reasons for which it is commonly difficult to detect UFOs in AGN. This suggests that we may currently underestimate their effects on to the surrounding medium through the process of feedback (see also Gaspari & Sadowski 2017), and that flux-resolved X-ray spectroscopy can be used to better detect and constrain the wind.

In a forthcoming paper we will extend this analysis to the archival data of the brightest AGN, with particular focus on the NLS1s that provide the statistics and the different flux states necessary to search for UFOs and study their variability. We expect future missions such as the *X-ray Astronomy Recovery Mission* (*XARM*) and *Advanced Telescope for High Energy Astrophysics* (*ATHENA*; Nandra et al. 2013) to revolutionize the way we study UFOs thanks to their microcalorimeter detectors, which possess high spectral resolution and effective area throughout the X-ray band.

6 CONCLUSIONS

In this work we have studied the UFO recently discovered in the NLS1 IRAS 13224, the most rapidly variable AGN in the X-ray energy band. We have found that the ionization parameter is correlated with the luminosity and, tentatively, the outflow velocity. In the brightest states the gas is almost completely ionized by the powerful radiation field and the UFO is hardly detected. This strengthens our recent results obtained with alternative

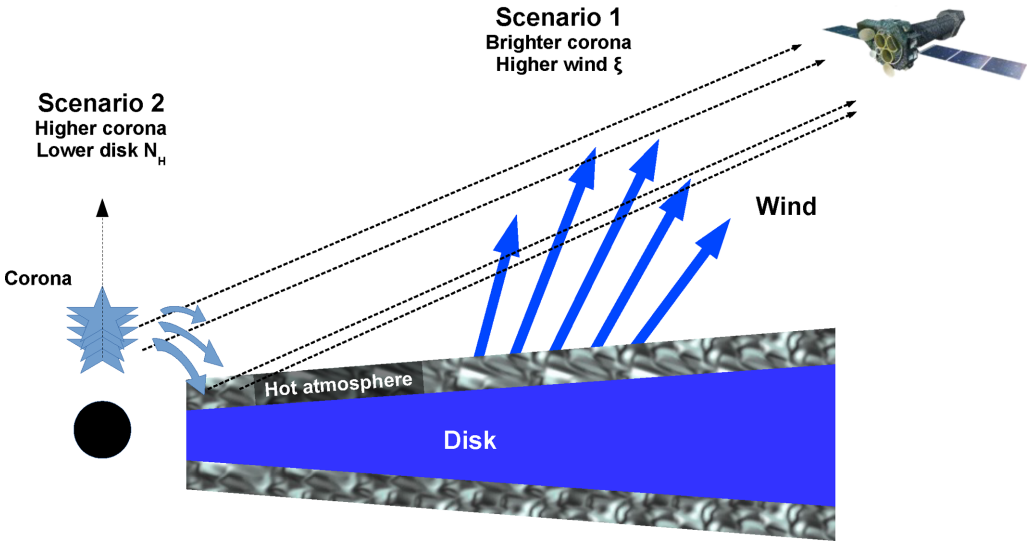

Figure 8. Possible scenarios of outflow response to the flux changes. Scenario 1: the X-ray source brightens, it overionizes the wind whose absorption lines weaken. Scenario 2: the average height of the corona increases and the corona brightens due to less light bending, the disc reflection decreases, and the corresponding absorption from the photosphere weakens compared to the relative source brightening.

techniques such as PCA. The high ionization of the outflowing gas may explain why it is commonly difficult to detect UFOs in AGN, suggesting that we may underestimate their contribution to AGN feedback.

ACKNOWLEDGEMENTS

This work is based on observations obtained with *XMM–Newton*, an ESA science mission funded by ESA Member States and USA (NASA). We also acknowledge support from ERC Advanced Grant Feedback 340442. WA acknowledges support from the European Union's Seventh Framework Programme (FP7/2013-2017) under grant agreement no. 312789, STRONGGRAVITY. DJKB acknowledges an STFC studentship. We also acknowledge support European Union's Horizon 2020 Programme under the AHEAD project (grant agreement no. 654215). We are grateful to Missagh Mehdipour for useful discussion on ionization balance and to the referee, Emanuele Nardini, for his useful comments that improved the clarity and quality of the paper.

REFERENCES

Blustin A. J., Fabian A. C., 2009, MNRAS, 399, 169
Buisson D. J. K., Lohfink A. M., Alston W. N., Fabian A. C., 2017, MNRAS, 464, 3194
Buisson D. J. K. et al., 2018, MNRAS, 475, 2306
Cappi M. et al., 2009, A&A, 504, 401
Chiang C.-Y., Walton D. J., Fabian A. C., Wilkins D. R., Gallo L. C., 2015, MNRAS, 446, 759
Dadina M., Cappi M., Malaguti G., Ponti G., de Rosa A., 2005, A&A, 442, 461
Dauser T. et al., 2012, MNRAS, 422, 1914
den Herder J. W. et al., 2001, A&A, 365, L7
Fabian A. C., 2012, ARA&A, 50, 455
Gallo L. C., Fabian A. C., 2011, MNRAS, 418, 59
Gallo L. C., Fabian A. C., 2013, MNRAS, 434, 66
Gallo L. C., Tanaka Y., Boller Th., Fabian A. C., Vaughan S., Brandt W. N., 2004, MNRAS, 347, 269
García J. A., Fabian A. C., Kallman T. R., Dauser T., Parker M. L., McClintock J. E., Steiner J. F., Wilms J., 2016, MNRAS, 462, 751
Gaspari M., Sądowski A., 2017, ApJ, 837, 149
Gupta A., Mathur S., Krongold Y., Nicastro F., 2013, ApJ, 772, 66
Gupta A., Mathur S., Krongold Y., 2015, ApJ, 798, 4
Hagino K., Odaka H., Done C., Tomaru R., Watanabe S., Takahashi T., 2016, MNRAS, 461, 3954
Jiang J. et al., 2017, MNRAS, submitted
Jin C., Ward M., Done C., Gelbord J., 2012, MNRAS, 420, 1825
Kaastra J. S., Bleeker J. A. M., 2016, A&A, 587, A151
Kosec P., Pinto C., Fabian A. C., Walton D. J., 2018, MNRAS, 473, 5680
Krongold Y., Nicastro F., Elvis M., Brickhouse N., Binette L., 2007, ApJ, 659, 1022
Longinotti A. L., Krongold Y., Guainazzi M., Giroletti M., Panessa F., Costantini E., Santos-Lleo M., Rodriguez-Pascual P., 2015, ApJ, 813, L39
Lumb D. H., Warwick R. S., Page M., De Luca A., 2002, A&A, 389, 93
Maiolino R. et al., 2017, Nature, 544, 202
Matzeu G. A., Reeves J. N., Braito V., Nardini E., McLaughlin D. E., Lobban A. P., Tombesi F., Costa M. T., 2017, MNRAS, 472, L15
Mehdipour M., Kaastra J. S., Kallman T., 2016, A&A, 596, A65
Nandra K. et al., 2013, preprint (arXiv:1306.2307)
Nardini E. et al., 2015, Science, 347, 860
Parker M. L. et al., 2017a, Nature, 543, 83 (P17a)
Parker M. L. et al., 2017b, MNRAS, 469, 1553 (P17b)
Pinto C., Kriss G. A., Kaastra J. S., Costantini E., Ebrero J., Steenbrugge K. C., Mehdipour M., Ponti G., 2012a, A&A, 541, A147
Pinto C., Ness J.-U., Verbunt F., Kaastra J. S., Costantini E., Detmers R. G., 2012b, A&A, 543, A134
Pinto C., Kaastra J. S., Costantini E., de Vries C., 2013, A&A, 551, A25
Pinto C., Middleton M. J., Fabian A. C., 2016, Nature, 533, 64
Ponti G., Fender R. P., Begelman M. C., Dunn R. J. H., Neilsen J., Coriat M., 2012, MNRAS, 422, 11
Porquet D., Dubau J., 2000, A&AS, 143, 495
Pounds K. A., 2014, MNRAS, 437, 3221
Reeves J. N. et al., 2014, ApJ, 780, 45
Reeves J. N., Braito V., Nardini E., Behar E., O'Brien P. T., Tombesi F., Turner T. J., Costa M. T., 2016, ApJ, 824, 20
Sani E., Lutz D., Risaliti G., Netzer H., Gallo L. C., Trakhtenbrot B., Sturm E., Boller T., 2010, MNRAS, 403, 1246
Steenbrugge K. C., Kaastra J. S., de Vries C. P., Edelson R., 2003, A&A, 402, 477
Takeuchi S., Ohsuga K., Mineshige S., 2013, PASJ, 65, 88
Tombesi F., Cappi M., Reeves J. N., Palumbo G. G. C., Yaqoob T., Braito V., Dadina M., 2010, A&A, 521, A57
Turner M. J. L. et al., 2001, A&A, 365, L27
Vasudevan R. V., Fabian A. C., 2007, MNRAS, 381, 1235
Vaughan S., Uttley P., 2008, MNRAS, 390, 421
Zoghbi A. et al., 2015, ApJ, 799, L24

APPENDIX A: ADDITIONAL PLOTS

Here we place some plots and tables that are excluded from the main body of the paper to facilitate the reading.

In Table A1 we report our continuum spectral fits to let the reader reproduce our results. The broad-band EPIC-pn spectra are fitted simultaneously to better constrain the parameters of the relativistic LAOR model that is coupled between the 10 spectral models. Each component is redshifted ($z = 0.0658$) and absorbed by interstellar gas ($N_{\rm H} = 6.75 \times 10^{20}$ cm^{-2}). The two iron lines are also broadened by a relativistic LAOR model with inner radius $1.35 \pm 0.01(GM/c^2)$, outer radius fixed to 400 (GM/c^2), emissivity slope (or index) 9.28 ± 0.04, and inclination $67\overset{\circ}{.}8 \pm 0\overset{\circ}{.}3$. We show the residuals to this fits in Fig. 2. We chose to fix the outer radius and to couple the Fe K line energy because the spectra are not sensitive enough to constrain them well. The parameters of the LAOR component have been fitted simultaneously to the 10 flux-resolved spectra (Table A2).

Figs A1 and A2 show the EPIC-pn and the RGS spectra extracted for the 10 flux-resolved intervals (νF_ν versus energy). They have been multiplied by constant values for display purposes.

We underline that these models are phenomenological and mainly useful to reproduce the continuum and the overall spectral shape. We refer to Jiang et al. (2017) for any discussion about the spectral decomposition and the study of the soft excess and the reflection and their trends with the flux. We just notice that the primary, power-law, component progressively softens with increasing flux, whilst the blackbody temperature increases. The energy of the Fe L line significantly increases with the flux most likely due to an increase of the disc ionization at high fluxes. Unfortunately, the spectra are not sensitive enough to constrain any trend in the Fe K line with the 10 spectra.

In Figs A3 and A4 we compare the SPEX default SED with the time-integrated average SED of IRAS 13224 and those for the flux intervals 1 and 10 (which are expected to be the most different ones). The stability curves are calculated with the SPEX XABSINPUT tool. There is very little deviation between SED and ionization balance calculated for different flux intervals. Moreover, the IRAS flux-resolved SEDs are averaged throughout several epochs and therefore do not take into account epoch-by-epoch variations. For these reasons, we preferred to use the SPEX default SED and

Table A1. Continuum spectral fits for the 10 flux-resolved EPIC-pn spectra.

Level	Power law		Blackbody		Fe L line		Fe K line	
	Norm (10^{52} photons s^{-1} keV^{-1})	Γ	Area (10^{23} cm^2)	kT (keV)	Norm (10^{51} photons s^{-1})	Energy (keV)	Norm (10^{50} photons s^{-1})	Energy (keV)
1	0.087 ± 0.007	2.189 ± 0.009	1.56 ± 0.02	0.1117 ± 0.0002	1.24 ± 0.02	0.872 ± 0.002	0.76 ± 0.03	7.37 ± 0.4
2	0.239 ± 0.002	2.348 ± 0.008	3.31 ± 0.07	0.1099 ± 0.0005	3.01 ± 0.03	0.892 ± 0.002	0.94 ± 0.05	7.37 coupled
3	0.360 ± 0.002	2.438 ± 0.008	3.87 ± 0.02	0.1102 ± 0.0006	3.57 ± 0.04	0.908 ± 0.002	0.99 ± 0.06	7.37 coupled
4	0.532 ± 0.003	2.563 ± 0.008	4.09 ± 0.09	0.1127 ± 0.0006	4.02 ± 0.05	0.916 ± 0.003	1.27 ± 0.07	7.37 coupled
5	0.741 ± 0.004	2.673 ± 0.008	4.4 ± 0.1	0.1125 ± 0.0003	4.74 ± 0.06	0.921 ± 0.003	1.5 ± 0.1	7.37 coupled
6	0.883 ± 0.004	2.690 ± 0.007	4.3 ± 0.1	0.1153 ± 0.0004	4.6 ± 0.1	0.935 ± 0.004	1.5 ± 0.1	7.37 coupled
7	1.081 ± 0.006	2.807 ± 0.008	4.6 ± 0.2	0.115 ± 0.001	5.3 ± 0.1	0.937 ± 0.005	1.8 ± 0.1	7.37 coupled
8	1.404 ± 0.007	2.792 ± 0.007	3.9 ± 0.1	0.120 ± 0.001	4.3 ± 0.1	0.967 ± 0.004	1.5 ± 0.1	7.37 coupled
9	2.096 ± 0.009	2.896 ± 0.006	3.3 ± 0.1	0.124 ± 0.001	4.4 ± 0.1	0.973 ± 0.005	2.2 ± 0.2	7.37 coupled
10	2.98 ± 0.01	2.833 ± 0.006	3.2 ± 0.1	0.132 ± 0.001	4.1 ± 0.2	0.996 ± 0.008	1.7 ± 0.2	7.37 coupled

Note. Each component is redshifted ($z = 0.0658$, which in SPEX corresponds to a distance of 296 Mpc) and absorbed by interstellar gas. The two iron lines are relativistically broadened. The Fe K line energy is coupled between all models.

Table A2. Photoionized absorber parameters for the two solutions.

Level	L_X (10^{43} erg s^{-1})	Fast solution N_H (10^{24} cm^{-2})	Fast solution log ξ log (erg cm s^{-1})	Fast solution v (c)	Slow solution N_H (10^{24} cm^{-2})	Slow solution log ξ log (erg cm s^{-1})	Slow solution v (c)
1	2.45	0.8 ± 0.2	4.20 ± 0.04	0.238 ± 0.005	7.5 ± 0.3	4.75 ± 0.04	0.212 ± 0.007
2	5.62	0.8 ± 0.2	4.16 ± 0.04	0.238 ± 0.005	7.2 ± 0.5	4.74 ± 0.04	0.210 ± 0.007
3	7.00	0.6 ± 0.2	4.24 ± 0.04	0.250 ± 0.006	7.2 ± 0.6	4.78 ± 0.04	0.215 ± 0.008
4	8.42	0.8 ± 0.1	4.20 ± 0.04	0.238 ± 0.005	6.9 ± 0.4	4.77 ± 0.03	0.211 ± 0.007
5	10.3	0.5 ± 0.2	4.26 ± 0.05	0.255 ± 0.008	5.8 ± 0.3	4.79 ± 0.04	0.221 ± 0.009
6	11.2	0.6 ± 0.2	4.31 ± 0.06	0.247 ± 0.007	6.7 ± 1.2	4.86 ± 0.04	0.22 ± 0.01
7	13.0	0.5 ± 0.2	4.34 ± 0.07	0.25 ± 0.01	6.6 ± 0.5	4.88 ± 0.04	0.22 ± 0.01
8	14.5	0.5 ± 0.3	4.6 ± 0.1	0.26 ± 0.01	6.1 ± 1.7	5.03 ± 0.06	0.23 ± 0.01
9	18.1	0.8 ± 0.5	4.5 ± 0.1	0.27 ± 0.01	5.9 ± 1.9	5.07 ± 0.07	0.24 ± 0.02
10	24.2	0.5 ± 0.3	4.8 ± 0.2	0.29 ± 0.03	8.7 ± 1.2	5.7 ± 0.3	0.26 ± 0.02

Note. X-ray luminosities (0.3–10 keV) are corrected for Galactic absorption and redshift ($z = 0.0658$), which in SPEX corresponds to a distance of 296 Mpc. The spectral fits are also shown in Figs A5 and A6. Line-of-sight velocities are in units of speed of light.

ionization balance in our fits, just like previously done in Parker et al. (2017a). The main (systematic) effect using SPEX rather IRAS 13224 (putative) flux-resolved SED is a shift of +0.5 in the log ξ of all our fits (as mentioned in Parker et al. 2017a). All trends are instead confirmed and at the same significance. We aim to obtain more detail on epoch-by-epoch effects in a forthcoming paper where we focus on time-resolved spectroscopy and time-resolved SED modelling (Figs A5 to A8).

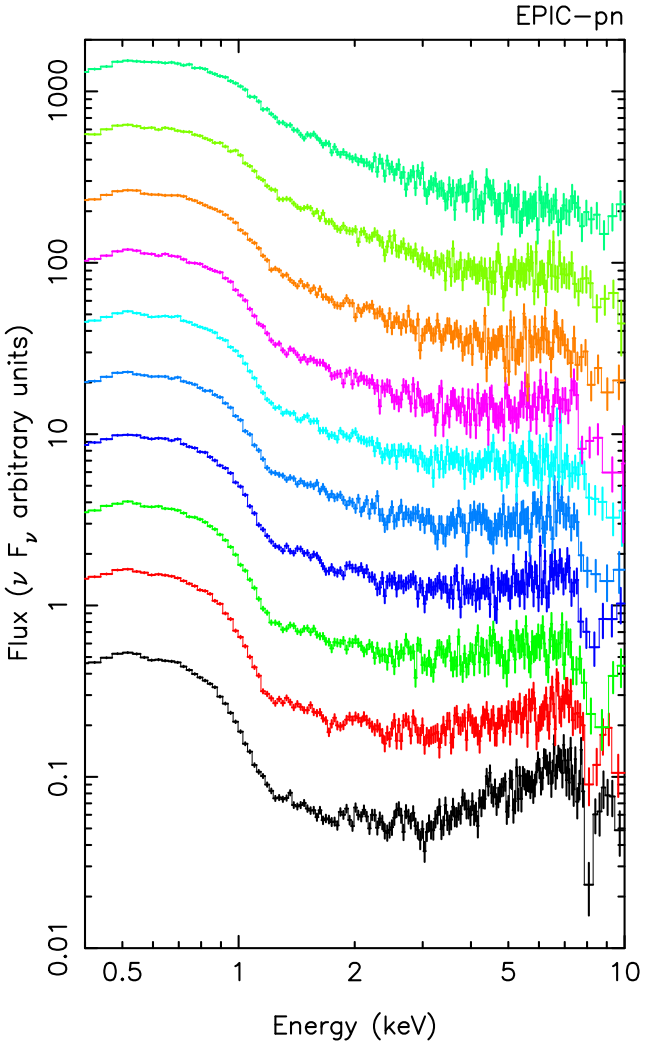

Figure A1. IRAS 13224 flux-selected EPIC-pn spectra (ordered according to increasing luminosity from bottom to top). The spectra have been shifted along the *Y*-axis for plotting purposes.

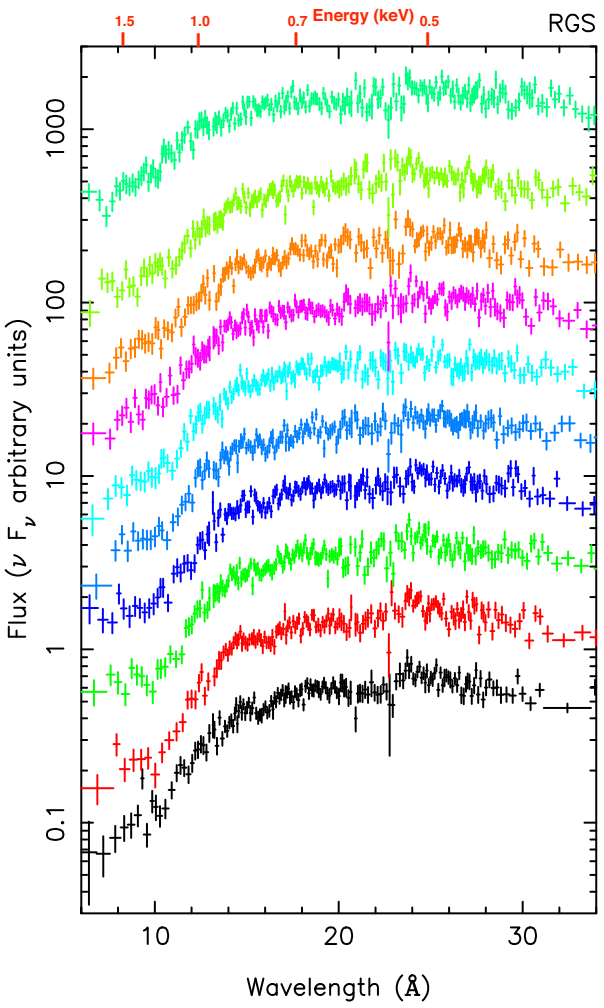

Figure A2. IRAS 13224 flux-selected RGS spectra (ordered according to increasing luminosity from bottom to top). The spectra have been shifted along the *Y*-axis for plotting purposes.

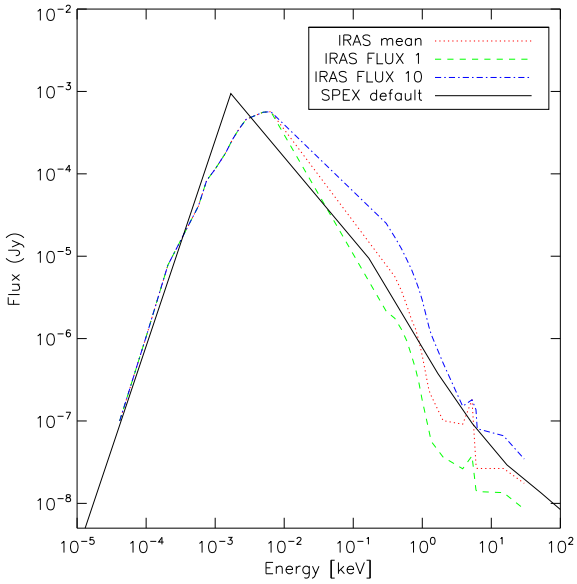

Figure A3. SED of IRAS 13224 lowest and highest flux intervals compared with the time average SED and the default SED used by SPEX (NGC 5548).

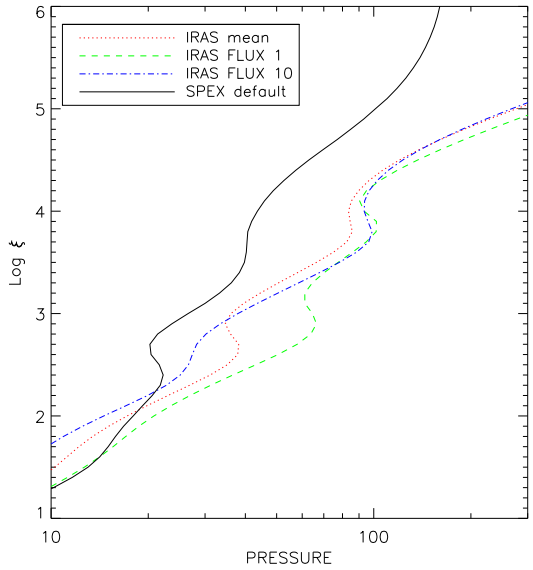

Figure A4. Stability curves of IRAS 13224 lowest and highest flux intervals compared with those for the time average SED and the default SED used by SPEX (NGC 5548, see Fig. A2). The pressure is defined as $\Xi = 19222\,\xi/T$ (Mehdipour, Kaastra & Kallman 2016).

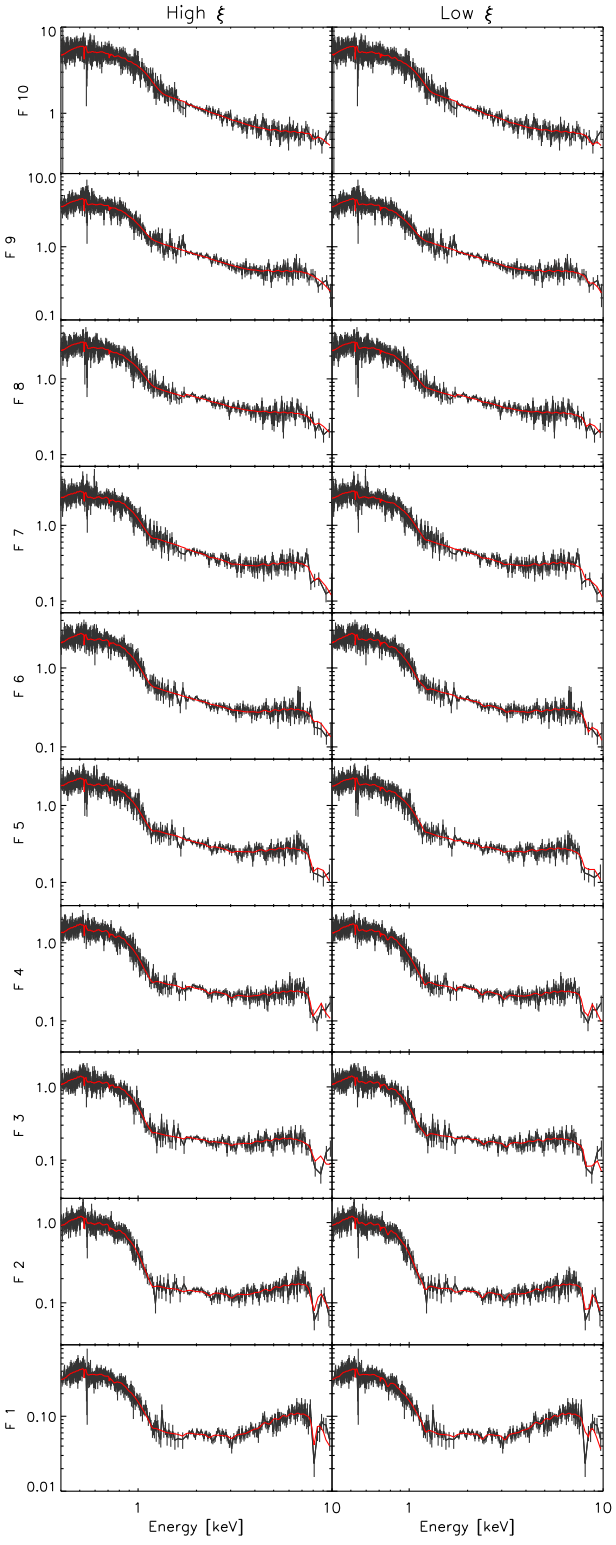

Figure A5. IRAS 13224 flux-selected RGS (<1.77 keV) and EPIC-pn (>1.77 keV) spectra (ordered according to increasing luminosity from bottom to top) with best-fitting models for the two solutions. *Y*-units are in counts $m^{-2}\,s^{-1}$ Å.

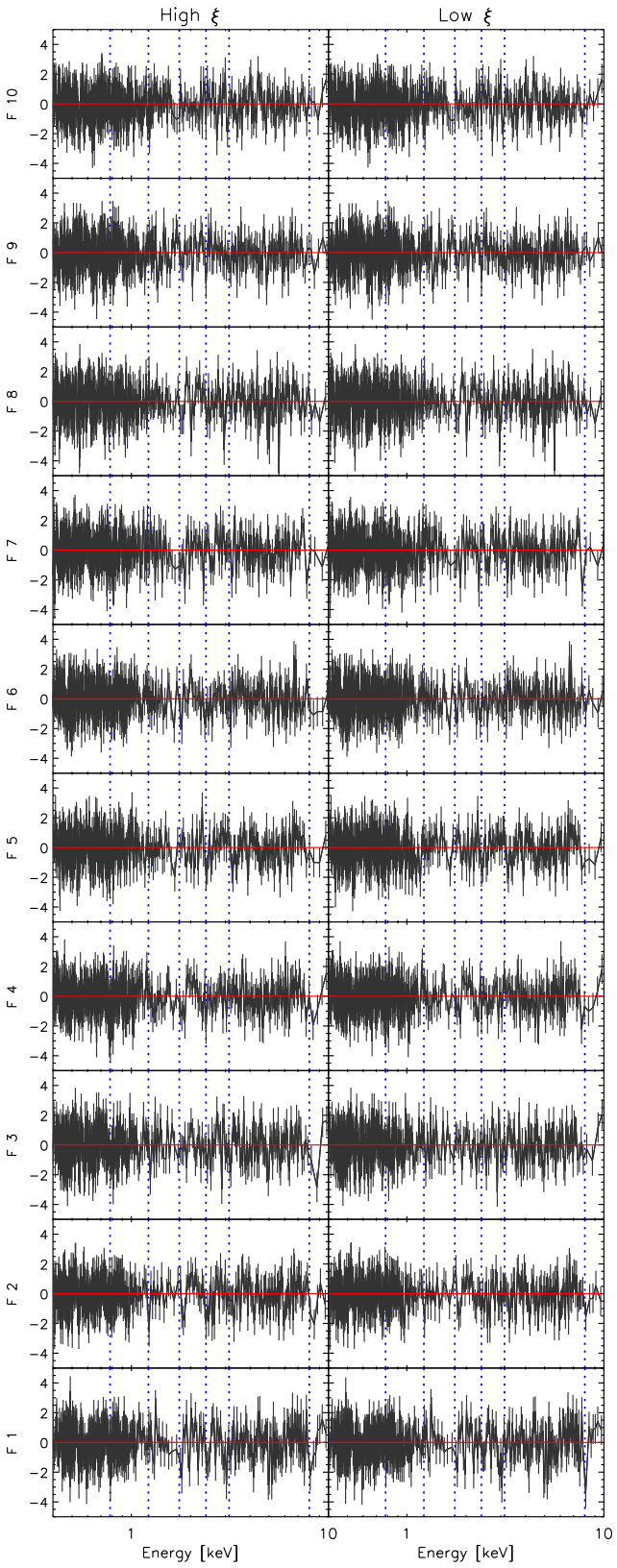

Figure A6. IRAS 13224 flux-selected RGS (<1.77 keV) and EPIC-pn (>1.77 keV) spectral residuals from the best-fitting models (see also Fig. A5).

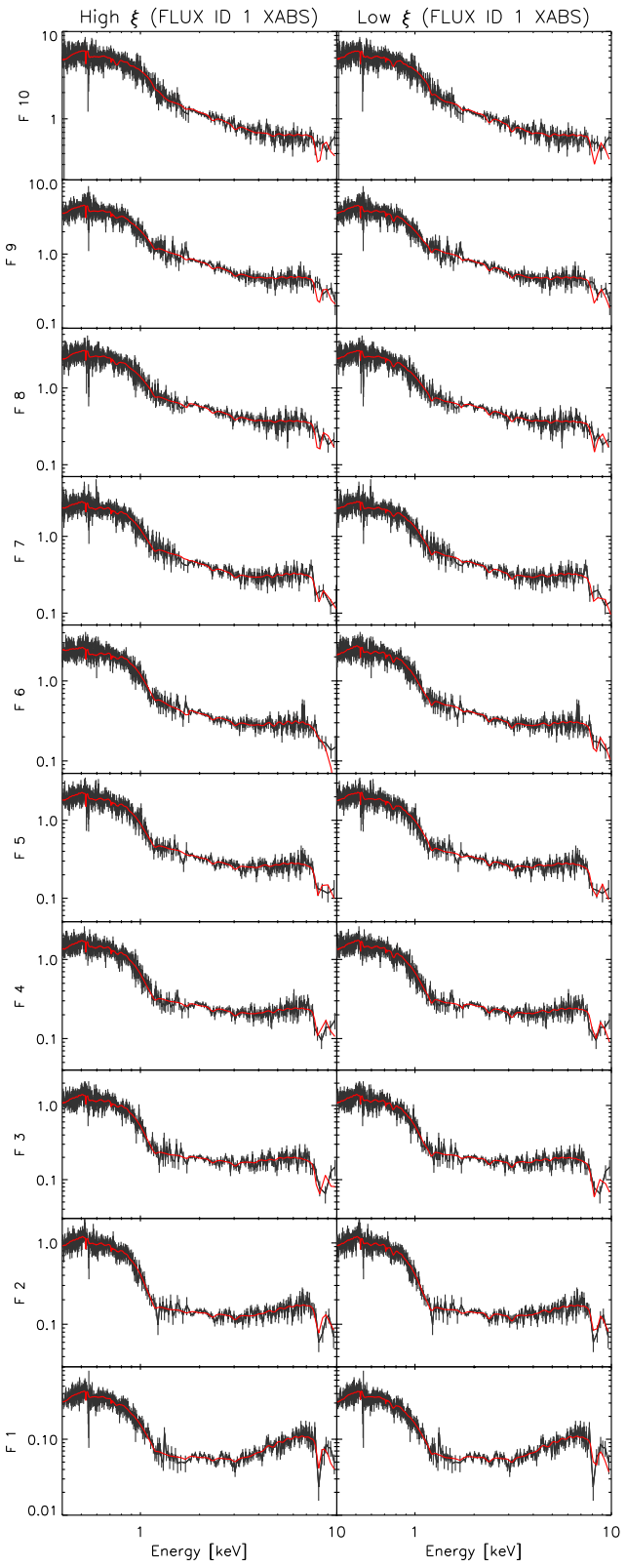

Figure A7. IRAS 13224 flux-selected RGS (<1.77 keV) and EPIC-pn (>1.77 keV) spectra (ordered according to increasing luminosity from bottom to top) with absorption model from the lowest flux spectrum. *Y*-units are in counts m^{-2} s^{-1} Å.

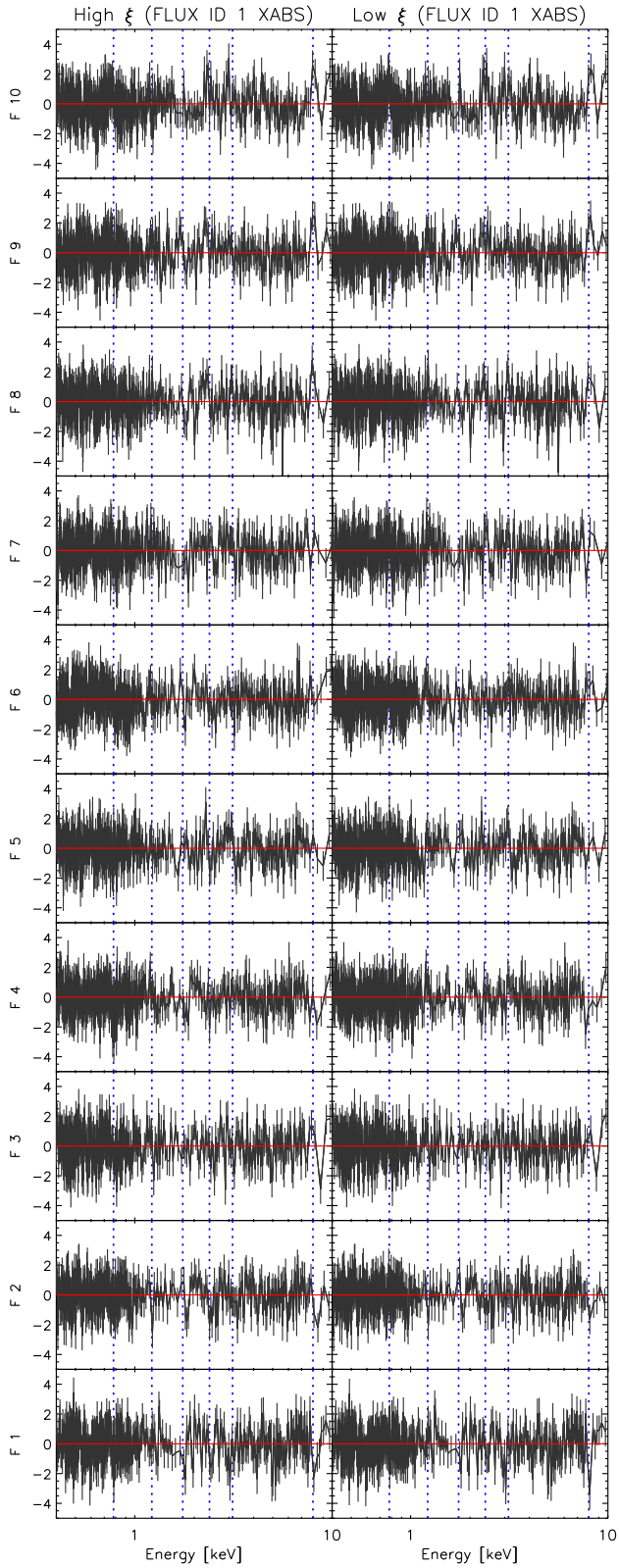

Figure A8. IRAS 13224 flux-selected RGS (<1.77 keV) and EPIC-pn (>1.77 keV) spectral residuals adopting the absorption model parameters from the lowest flux spectrum (see Fig. A7).

This paper has been typeset from a TEX/LATEX file prepared by the author.